The 2021 Mw8.1 Kermadec Megathrust Earthquake: An Event Rupturing the Slab-Mantle Interface With Up-Dip High-Frequency Seismic Energy Radiation

Hongyu Zeng[1,2] [iD], **Shengji Wei[1,2,3]** [iD], **and Hongfeng Yang[4]** [iD]

[1]Asian School of the Environment, Nanyang Technological University, Singapore, Singapore, [2]Earth Observatory of Singapore, Nanyang Technological University, Singapore, Singapore, [3]Key Laboratory of Deep Petroleum Intelligent Exploration and Development, Institute of Geology and Geophysics, Chinese Academy of Sciences, Beijing, China, [4]Earth System Science Programme, The Chinese University of Hong Kong, Shatin, China

Abstract Megathrust earthquakes often break the slab-crust interface and radiate high-frequency seismic waves from the down dip of their coseismic slip. In contrast, we show that the 2021 Mw8.1 Kermadec earthquake deviates from this mode. We resolve the kinematic rupture process of the event by leveraging finite fault inversions and a calibrated tele-seismic back-projection imaging method. The finite fault inversions reveal a compact slip patch with a ∼7-m peak slip of the earthquake located on the slab-mantle interface at the depth of 20–50 km, while the back-projection shows the high-frequency energy was radiated from ∼20 km depth along the updip edge of the slip patch, and coinciding with the slab-forearc Moho intersection. The rougher frictional patches responsible for high-frequency radiation are likely caused by strong material contrast transitioning from slab-crust to slab-forearc mantle contacts. Significant slip on the slab-mantle contact necessitates a re-evaluation of earthquake hazards in conventionally considered aseismic regions.

Plain Language Summary Megathrust earthquakes result from abrupt shear dislocations, or ruptures, on the interfaces between subducting slabs and overriding plates. Traditionally, these earthquakes are believed to rupture the interface between the slab and the overriding crust, with high-frequency seismic waves—which are particularly damaging to infrastructure—originating from the deeper parts of these ruptures. However, our study of the 2021 Mw8.1 Kermadec earthquake, occurring at the interface between the subducting Pacific and the overriding Australian plates, challenges this conventional view. Our analysis shows that this event primarily ruptured the interface between the slab and the overriding mantle, and the high-frequency waves were primarily emitted from the shallowest part of the rupture, closely aligning with the depth of the boundary between the overriding crust and mantle. This alignment suggests that frictional heterogeneity at this depth, related to the transition from slab-crust to slab-mantle interfaces, significantly influences the generation of high-frequency waves. These findings broaden our understanding of seismic capabilities on the plate interface and underscore the need for refined seismic hazard assessments globally.

1. Introduction

The largest and most destructive earthquakes, which are capable of generating damaging ground shaking and tsunamis, occur along subduction zone plate interfaces. Seismic and geodetic observations of megathrust earthquakes have revealed systematic patterns of frequency-dependent energy radiation (Asano & Iwata, 2012; Avouac et al., 2015; Lay et al., 2012; Simons et al., 2011; Yao et al., 2013; Yin et al., 2016). These studies indicate that low-frequency seismic waves are predominantly generated in the central or shallow parts of the coseismic rupture, while coherent high-frequency (HF) seismic waves emanate primarily from the deeper, lower edges, suggesting along dip/depth-varying frictional properties on the plate interface (Lay et al., 2012; Yao et al., 2013).

The shallow (∼0–15 km) and intermediate depth (∼15–35 km) sections of the plate interface are known as tsunamigenic and main seismogenic zones, respectively, exhibiting depleted and intermediate HF radiation during the coseismic rupture. In contrast, the deeper section (typically ∼35–55 km) acts as the seismic-aseismic transition zone, characterized by more heterogeneous frictional/stress patches, which result in relatively small slip but intense HF energy radiation. These depth-dependent rupture characteristics can be attributed to variations in fault zone properties, including temperature, pore fluid pressure (Kodaira et al., 2004), fault geometry (X. Wang

Writing – original draft: Hongyu Zeng,
Shengji Wei
Writing – review & editing:
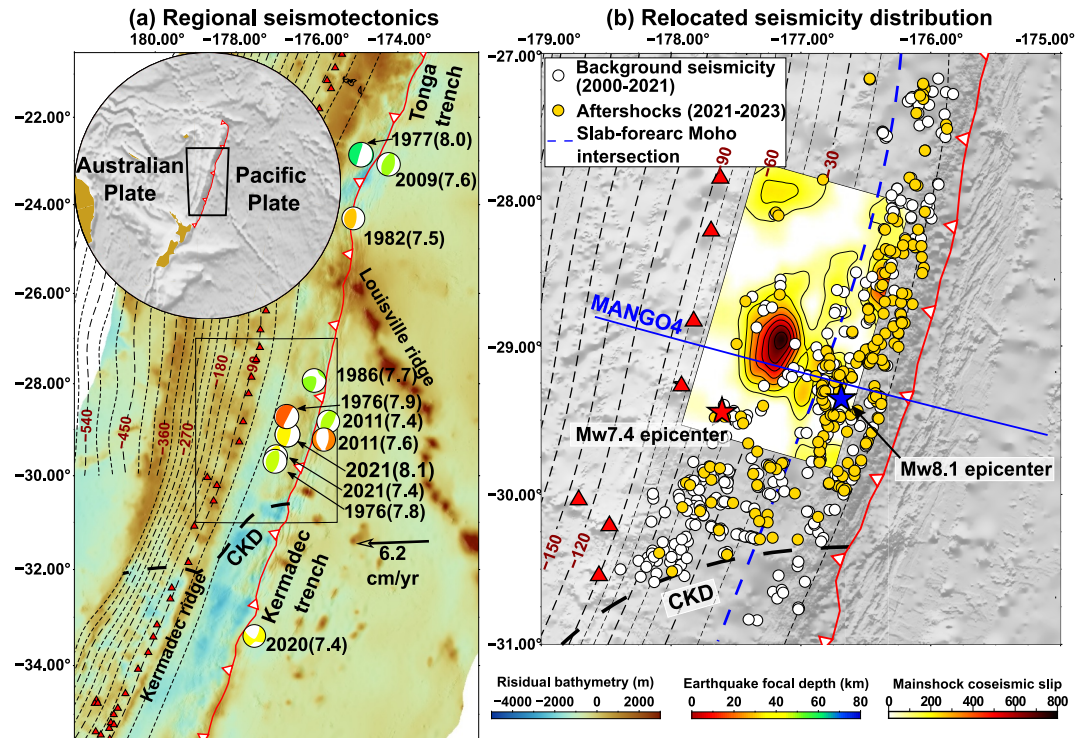Hongyu Zeng, Shengji Wei,
Hongfeng Yang

Figure 1. Seismo-tectonic overview of the Kermadec subduction zone. (a) Overview of the Australian-Tonga-Kermadec subduction. Beachballs show earthquakes with magnitude >7.4 since 1976 from the GCMT catalog. The background color indicates the residual bathymetry, the bathymetry relative to the trench perpendicular average component in a subduction zone (D. Bassett & Watts, 2015). CKD represents the Central Kermadec Discontinuity (Dan Bassett et al., 2016), which is featured with strong residual bathymetry anomaly. Red triangles denote the fore-arc volcanoes. Dashed contours mark the depth of slab2.0 interface (Hayes et al., 2018). (b) Relocated seismicity with shallow-dipping thrust focal mechanism ($M < 7.0$, 2000–2023) (Ekstrom et al., 2012). Colored patches and black contours (with an interval of 1 m) show the coseismic slip distribution of the mainshock. MANGO4 is the seismic reflection and refraction profile in Bassett et al. (Dan Bassett et al., 2016). Heavy blue dashed line denotes the intersection between the slab2.0 model (Hayes et al., 2018) and the forearc Moho, assuming a forearc Moho depth of 17 km (Dan Bassett et al., 2016).

et al., 2017], rigidity (Sallarès & Ranero, 2019), as well as rock types and mineral phases (Hacker et al., 2003) along the plate interface.

Notably, the down-dip extent of the seismogenic zone—a key parameter determining the maximum magnitude of potential catastrophic megathrust earthquakes—is proposed to be controlled either thermally or compositionally (Hyndman & Peacock, 2003; Hyndman et al., 1997), dependent on whether the ~350°C isotherm or the serpentinized mantle is shallower. The former marks the brittle-to-ductile transition, while the latter is associated with velocity-strengthening friction of serpentinites that tend to release stress through aseismic slips. While large megathrust earthquakes (e.g., the 2011 Tohoku-Oki earthquake), occasionally penetrate into the slab-mantle fault interface, the majority of coseismic slip typically occurs at the slab-crust interface.

However, these observations and interpretations have primarily focused on megathrusts with a continental overriding plate. It remains unclear whether megathrust between two oceanic plates show similar along-dip variations. The 4th March 2021 Mw8.1 Kermadec megathrust earthquake, occurring along an oceanic-oceanic plate interface, provides a unique opportunity to explore this question. The Mw8.1 event resulted from the fast subduction (~6 cm/yr (DeMets et al., 2010)) of the older (~100 Myr (Müller et al., 2008)) Pacific plate beneath the overriding Australian plate (Figure 1a). The mainshock, with a relatively deep centroid depth of 33.9 km and preceded by an even deeper Mw7.4 foreshock at a depth of 44.8 km according to Global Centroid Moment Tensor (GCMT) report (Dziewonski et al., 1981; Ekstrom et al., 2012), primarily ruptured the fault interface beneath the forearc Moho that has a depth of ~17 km (Figure 1b). This depth feature differentiates it from many other large megathrust earthquakes that mostly ruptured slab-crust fault interface (Hyndman et al., 1997; Simons et al., 2011; K. Wang et al., 2020; Yin et al., 2016). For instance, the 2011 Mw9.1 Tohoku-Oki earthquake nucleated near the

slab-forearc Moho intersection at ∼21 km (Miura et al., 2005) with most of its slip occurred updip of the hypocenter (Uchida & Bürgmann, 2021). The peak slip of the 2014 Mw8.1 Iquique earthquake is located at the depth of ∼25 km (Ruiz et al., 2014), while forearc Moho of the overriding plate is possibly deeper (Yuan et al., 2000). Similarly, the 2016 Mw7.6 southern Chile earthquake primarily ruptured in the 20–35 km depth range on the plate interface, shallower than the slab-Moho intersection (Moreno et al., 2018).

To better understand the fault property of the 2021 Kermadec event, we resolve the mainshock kinematic rupture process by deriving coseismic slip models using finite fault inversion (FFI) and tracking HF spatial and temporal evolution using back-projection (BP) analysis. The joint analysis reveals that the mainshock primarily ruptured the slab-mantle interface and radiated HF energy from the updip edge of the coseismic slip, indicating a new mode of seismogenic environment on this oceanic-oceanic subduction zone plate interface.

2. Methods

2.1. Finite Fault Inversion

We resolve the coseismic rupture process of the mainshock by conducting FFI using teleseismic data (Ji et al., 2002). We adopt the strike (196°) and dip (19° to west) angles of the fault plane from the GCMT focal solution. To better constrain the absolute location of the mainshock coseismic slip, we also incorporate seafloor vertical deformation data derived from tsunami waveform modeling (Romano et al., 2021) into the FFI (Figure S3; see more in Supporting Information S1), and assign equal weights to the seismic and seafloor vertical deformation data set. Prior to the FFI, we refine the mainshock hypocenter using a travel time calibration method (detailed in Section 2.3). The preferred slip model is shown in Figure 2b, with the fits of teleseismic waveforms and seafloor vertical deformation shown in Figures S2 and S3 in Supporting Information S1, respectively.

2.2. Surface Wave Relocation of Moderate Size Earthquakes

To enhance the accuracy of BP imaging, we implement a travel-time path calibration (Zeng et al., 2022) to mitigate the effects of the source-side 3D velocity structure on teleseismic travel times (detailed in Supporting Information S1). Travel-time calibration for a teleseismic array could be achieved by using records from well-located moderate size (e.g., Mw5.5–7.0) earthquakes in and around the mainshock rupture area. However, a high-resolution earthquake catalog is not available in the Kermadec region due to lacking regional seismic network. In the global earthquake catalogs, such as the GCMT and National Earthquake Information Center (NEIC) (https://earthquake.usgs.gov/earthquakes/search/), location discrepancies for the same event often exceed 50 km (Figures S5a and S8a in Supporting Information S1).

To derive a higher resolution catalog for moderate size earthquakes in and around the mainshock rupture area, we employ a surface wave relative relocation method (Figure S4 in Supporting Information S1) (Xin Wang et al., 2018), proven to reduce earthquake horizontal location uncertainty to less than 10 km, despite that the seismic stations used are all located beyond the regional distances (Xin Wang et al., 2024). We use this method to relocate all shallow-dipping thrust events with magnitude smaller than 7 in the GCMT catalog since 2000. We select an event with consistent horizontal locations in the NEIC and GCMT catalogs, and with a depth consistent with the Slab2.0 model (2021-03-05T14:24, Figure S8a in Supporting Information S1) (Hayes et al., 2018; K. Lythgoe et al., 2023), as the initial reference event to relocate the other events. The arrival times of surface waves from other events relative to the reference event at a common station can be precisely estimated if their waveforms are highly similar. The relative arrival time is therefore measured by finding the maximum cross-correlation coefficients between the surface waves from the reference and target events (Figure S4a in Supporting Information S1). The obtained relative arrival times then are used to relocate target events with high resolution (Figure S4c in Supporting Information S1) (more details in the **SI**).

To refine the centroid depths of the relocated events, we improve the identification of depth phases and the accuracy of arrival time picks, which are used to update the depth estimates of some earthquakes (more details in Supporting Information S1). Eventually, a total of 545 events are relocated, including background seismicity and the 2021 aftershocks (Figure S9 in Supporting Information S1). The new catalog also agrees better with the Slab2.0 plate interface model and the slab interface derived from the seismic profile in the study area (MOGO4 in Figure 1b) (Dan Bassett et al., 2016) (Figure S9c in Supporting Information S1).
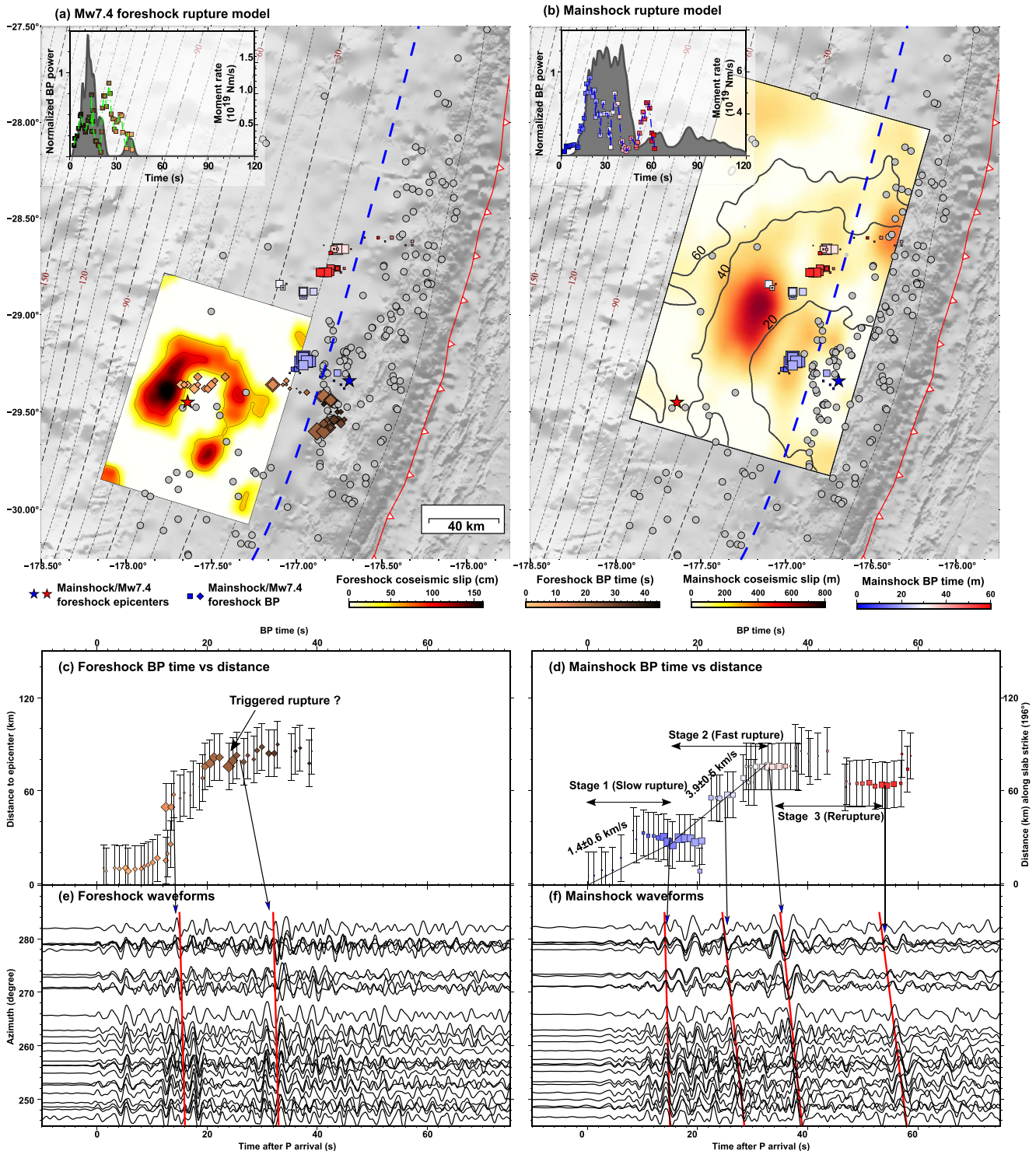
Figure 2. Kinematic rupture models for the Kermadec Mw7.4 foreshock and mainshock. (a) Map view of the coseismic slip (color patches) and BP result (diamonds) for the Mw7.4 foreshock (K. Lythgoe et al., 2023). Black dashed lines represent the slab2.0 model. Heavy blue dashed line denotes the intersection between the slab and the forearc Moho. (b) Same as (a) but for the mainshock. Insets in (a) and (b) are moment rate functions for the two events, plotted with BP beamforming power shown as dashed lines. Gray circles in (a)–(b) denote relocated thrust aftershocks. Red and blue stars are epicenters of the foreshock and mainshock determined from BP. Black contours in the mainshock slip model show the rupture time (c)–(d) BP results shown as time and distance (to the relocated epicenter) relation for the foreshock and mainshock (e)–(f) HF velocity waveforms (0.3–1.0 Hz) of the foreshock and mainshock recorded by the Australian array. Arrows connect the imaged HF clusters and the corresponding coherent wave trains. In estimating the speed of the second stage of the mainshock rupture, we project the HF radiators to the slab strike and then the distances are measured.

2.3. Tele-Seismic Back-Projection

To resolve the detailed spatial-temporal HF (0.3–1.0 Hz) evolution of the mainshock and the Mw7.4 forshock, we conduct a path calibrated BP analysis. BP takes advantage of source-receiver reciprocity and back-propagates the array HF waveform data to the source region, tracing the location and time of sources by either maximizing the stacking power in time domain (Ishii et al., 2005) or the coherence in frequency domain (Meng et al., 2011). However, the BP results may suffer from large uncertainties because the travel time, which is used to back-propagate HF waveforms, calculated using a 1D velocity model may not be accurate due to 3D source-side velocity structure (Zeng et al., 2022). To lessen the source-side 3D structure effect on the travel time calculation, we adopt a travel-time path calibration scheme, in which travel time correction is made by using the travel time of well-relocated, or calibration, events in the source region (Zeng et al., 2022).

The waveform data used for BP analysis are downloaded the only available large-aperture array located at a teleseismic distance (30–90°). Three relocated moderate-size events around the mainshock rupture area are selected for travel-time path calibrations (detailed in Supporting Information S1). The effectiveness of the calibration is verified by locating all moderate-sized events using the calibrated BP method and comparing the BP locations with those in the refined catalog (Figure S10 in Supporting Information S1). The agreement between the BP and catalog locations is remarkable (Figure S10c in Supporting Information S1), with an average discrepancy of ~12.5 km, which is considered as the location uncertainty in the BP results for the mainshock and its Mw7.4 foreshock.

3. Coseismic Slip Model, Relocated Seismicity and High-Frequency Radiation

3.1. Coseismic Slip Located at the Slab-Mantle Interface

The preferred slip model for the mainshock reveals a compact patch with a peak slip of ~7 m, situated at the depths of 20–50 km and extending ~100 km along the strike (Figure 2b). The moment-rate function (inset Figure 2b) indicates a 10-s weak initial rupture, followed by a dominant pulse with 40-s duration, corresponding to the compact slip patch and relatively simple teleseismic waveforms (Figure S2 in Supporting Information S1). Compared to the slip model without constraints from seafloor deformation (K. Lythgoe et al., 2023), the new model exhibits a larger peak slip due to the constraints from tsunami-derived seafloor deformation. The finite fault model for the Mw 7.4 foreshock also exhibits a relatively compact slip distribution (K. Lythgoe et al., 2023), located southwest of the mainshock, and showing spatial complement to the mainshock slip (Figure 2a).

3.2. Relocated Seismicity

Our refined earthquake catalog shows an active seismicity belt up dip to the mainshock rupture area (Figure 1b), their along dip separation is roughly corresponding to Moho depth of the overriding plate. Although the refined mainshock epicenter is also located in this seismicity belt, the mainshock rupture and its downdip areas exhibit much less background and aftershock seismicity (Figure 1b). This suggests a different frictional property of the plate interface between the mainshock rupture area and its up dip region, where the former is more uniformly locked, mostly rupturing as large events, while the latter has more heterogeneous coupled patches and stress distribution that produce more frequent smaller events.

3.3. Updip High-Frequency Radiation

The BP result of the mainshock indicates that its initial rupture (i.e., the first ~10 s) is located ~70 km northeast of the NEIC epicenter, while the initial rupture of the Mw7.4 event is placed ~30 km away from its NEIC epicenter (Figure S1b in Supporting Information S1). These location differences are substantially larger than the BP location uncertainty and resemble the discrepancies between the NEIC and our refined catalogs (Figure S5a in Supporting Information S1). The BP-inferred initial rupture locations of these events are considered as their relocated epicenters, which were used in their finite fault inversions.

Based on our BP results and finite fault models, the foreshock rupture (Figure 2a) initiated ~140 km west of the trench, corresponding to a depth of ~50 km on the plate interface assuming slab2 model. This is followed by a relatively simple slip patch that produces the peak of the moment release. About 17 s after the initial rupture, a HF radiation cluster, corresponding to the wave train ~26–41 s after the first P arrival (Figures 2a–2c and 2e), emerged ~80 km east of the Mw7.4 epicenter. The location of this cluster is distant from the major slip patch and

its timing appears ∼10 s later than the peak in the moment rate function (Figure 2a inset). Therefore, it likely represents an instantaneous, dynamically triggered updip rupture characterized by intense HF energy but negligible slip. Notably, its proximity to the mainshock epicenter suggests that dynamic stress perturbations from the foreshock may have facilitated the nucleation of the mainshock that occurred ∼2 hr later.

For the Mw8.1 mainshock, the BP result reveals a three-stage rupture process (Figures 2b and 2d). Initially, the rupture started ∼50 km west of the trench and propagated westward, or down-dip, at a speed of ∼1.4 km/s and lasted for ∼12 s. At the end of this stage, a strong HF radiation cluster burst ∼20 km west of the epicenter, persisting for ∼14 s, corresponding to the wave train 10–24 s after the first P arrival (Figures 2b–2d and 2f). In the second stage (∼20–40 s), the rupture propagated northward along the updip boundary of the coseismic slip at a speed of ∼3.9 km/s. In the final rupture stage (∼40–50 s), a prominent HF cluster appears ∼15 km south of the preceding HF cluster, suggesting a possible backward rupture or triggered re-rupture.

A notable feature of the mainshock rupture is that all HF sources are positioned along the updip boundary of the coseismic slip (Figure 2b). Given that the BP uncertainty is significantly smaller than the along-dip extent (∼60 km) of the mainshock slip, whose absolute location is well-constrained by the tsunami data (Romano et al., 2021), this updip HF radiation appears to be a robust feature of mainshock rupture. Moreover, all the mainshock HF sources lie along the base of the updip seismicity belt, indicating a heterogeneous stress and frictional state on the shallow (∼10–20 km in depth) portion of the plate interface, in contrast to a more homogeneous stress condition in the mainshock slip area (∼20–50 km depth).

The BP results in frequency bands 0.1–0.5 and 0.5–1.5 Hz (Figures S12a, S12c in Supporting Information S1) are consistent with that in the 0.3–1.0 Hz band, with HF radiators predominantly located along the up dip edge of the coseismic slip. The earthquake exhibits frequency-dependent rupture characteristics across these frequency bands, as illustrated by the waveforms and BP results (Figures S12b, S12d, S12e in Supporting Information S1). For instance, coherent wave pulses are observed after 40 s in the 0.1–0.5 and 0.5–1.5 Hz bands, whereas such features are nearly absent in the 0.5–1.5 Hz band.

4. Discussion and Conclusion

The Tonga-Kermadec subduction zone features a shallow forearc Moho, intersecting the subducting slab at a depth of ∼17 km in the 2021 mainshock rupture area (Dan Bassett et al., 2016; Contreras-Reyes et al., 2011; Stratford et al., 2015). Consequently, unlike most megathrust earthquakes ($M > 7.5$), which typically generate the majority of coseismic slip at the slab-crust interface, the majority of the Mw8.1 mainshock's coseismic slip occurred at the slab-mantle interface. But note that there are a few megathrust events also have significant portion of coseismic slip penetrating into slab-mantle interface, such as the 2007 Mw7.7 Tocopilla earthquake (K. Wang et al., 2025), the Mw7.7 aftershock of the 2014 Iquique earthquake (K. Wang et al., 2025) and the 2020 Mw7.8 Alaska earthquake (Shillington et al., 2022). In the 2021 Kermadec rupture area, GNSS data actually supports a high degree of seismic locking at the slab-mantle interface (Power et al., 2012). These observations challenge the traditional view that serpentinized mantle controls the down-dip limit of the seismogenic zone when temperatures are below ∼350°C (Figure 3) (Hyndman & Peacock, 2003; Hyndman et al., 1997). Our results suggest either the degree of serpentinization in the forearc mantle wedge is limited, or that serpentinites do not always exhibit velocity-strengthening friction, which promotes stable aseismic sliding (Hyndman & Peacock, 2003; Oleskevich et al., 1999).

Pervasive forearc mantle serpentinization in the Tonga-Kermadec subduction zone has been elucidated by seismic reflection/refraction investigations, revealing lower P-wave speeds compared to the dry mantle (Abers et al., 2017; Dan Bassett et al., 2016). Particularly, the MOGO4 seismic profile near the 2021 mainshock rupture indicates a forearc mantle P-wave velocity of ∼7.8 km/s, slower than the typical 8–8.4 km/s of a dry mantle. Given the relatively low temperature in the Kermadec subduction zone (Figure 3) (Gao & Wang, 2014), this reduction in P-wave velocity is most likely due to partial serpentinization of the forearc mantle, estimated at about 30% in Abers et al. (2017). Laboratory studies demonstrate that serpentinites can exhibit both velocity-strengthening (D. E. Moore and Lockner, 2013] and velocity-weakening (Biemiller et al., 2020; Kaproth & Marone, 2013) frictional properties under varied experimental conditions such as loading rate, temperature, and pore fluids. Furthermore, even slight serpentinization (greater than 10%–15%) has been shown to significantly influence fault friction (Escartin et al., 2001). These laboratory studies along with our observations of the 2021 Kermadec rupture suggest that the partially serpentinized mantle could display velocity-weakening behavior on
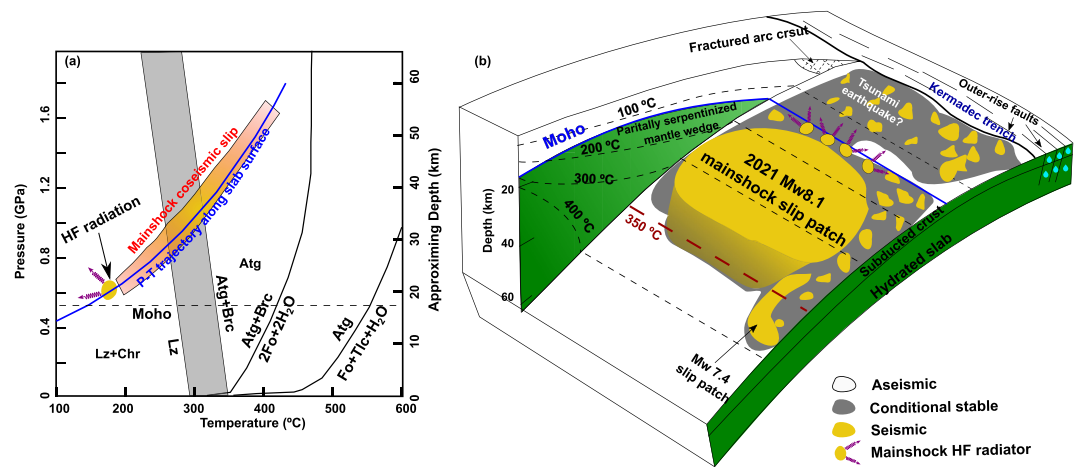
Figure 3. Schematic illustration of the seismogenic environment on Kermadec subduction zone. (a) Phase diagram of serpentine minerals adapted from Evans (Evans, 2004) and Schwartz et al. (Schwartz et al., 2013). The blue line denotes the P-T trajectory along the Kermadec slab surface from Gao and Wang (Gao & Wang, 2014). The dashed line marks the Moho depth determined in Bassett (Dan Bassett et al., 2016). Atg = Antigorite, Brc = Brucite, Chr = Chrysotile, Fo = Forsterite, Lz = Lizardite, $SiO_2(aq)$ = Silica in aqueous fluid, Tlc = Talc. The gray shaded area highlights the possible uncertainty in the transition from Lz to Atg + Brc. (b) Conceptual model proposed for the 2021 Mw 8.1 Kermadec earthquake sequence. Temperature contours (dashed lines) are adapted from Gao and Wang (Gao & Wang, 2014). Isolated frictional patches are introduced around forearc Moho during transitioning from slab-crust to slab-mantle contacts and are broken to promote HF radiation, while on the slab-mantle interface, the large patch is broken during the mainshock, emanating little HF radiation. In the down dip, there is a smooth brittle-to-ductile transition, inferred from the lack of down-dip HF radiation and background/aftershock seismicity. On the slab-crust contact (corresponding to the tsunamigenic domain in Lay et al. (Lay et al., 2012)), a large slip patch may exist and been broken as a tsunami or tsunamigenic earthquake, similar to the 2006 Mw 8.1 Kuril Islands earthquake (Lay et al., 2009).

the plate interface, thereby facilitating strong seismic coupling and substantial coseismic slip in a megathrust event.

Unlike many other megathrust earthquakes, the 2021 Kermadec mainshock radiated HF seismic energy primarily from the updip of the coseismic slip. Notably, the HF radiators, when projected onto the plate interface, coincide with the slab-forearc Moho intersection at ∼20 km depth (Figures 2b and 3b). This intersection marks a transition zone characterized by strong material contrasts due to the transition from slab-crust to slab-mantle contacts, resulting in pronounced stress and/or frictional heterogeneities (Figure 3b). Additionally, the location of the HF sources aligns with the ∼150°C isotherm (Figures 3a and 3b), roughly corresponding to the dehydration temperature of clay minerals [Hyndman et al., 1997; Ma et al., 2022; J. C. Moore and Vrolijk, 1992]. If abundant clay minerals present along the shallow plate interface, this material transition may further contribute to the stress and frictional heterogeneities. The breaking of isolated frictional patches within the heterogeneous transition zone could have radiated intense HF seismic energy during the mainshock (Huang et al., 2012; Lay et al., 2012).

Along the slab-crust interface updip of the 2021 mainshock rupture, we observe frequent background and aftershock seismicity as well as the mainshock epicenter, indicating more heterogeneous friction and/or stress compared with the deeper plate interface (Figure 3b). The slab-crust interface might occasionally rupture as a large event, generating devastating tsunamis, such as the 2006 Mw8.3 Kuril Island earthquake that also occurred on the oceanic-oceanic subduction zone plate interface (Lay et al., 2009). Insights into potential tsunami hazards from shallow plate interfaces can be gained by analyzing outer-rise and trench-slope earthquakes (Christensen & Ruff, 1988; Lay et al., 1989), although such analysis is beyond the scope of this paper.

The down dip cessation of the mainshock coseismic slip roughly matches the ∼350°C isotherm (Figure 3a), where mainshock HF radiation, background seismicity and aftershocks are also absent. These observations suggest a thermal control on the down-dip extent of the seismogenic zone (Karen Lythgoe et al., 2021; Omuralieva et al., 2012; Sibson, 1983) and a smooth brittle-to-ductile transition at the bottom of the mainshock rupture area. The Mw7.4 foreshock coseismic rupture penetrated even deeper part of plate interface than the mainshock,

accompanied by abundant seismicity at depths of ∼50–60 km nearby. This suggests along strike variation of frictional conditions, possibly related to changes in the forearc structure (K. Lythgoe et al., 2023].

Our approaches and findings have significant implications for global seismic hazard re-evaluation. We observed that the large slip patch of the 2021 Kermadec mainshock is located in an area nearly devoid of background seismicity (Figures 1b and S9a in Supporting Information S1). Similar long-term seismic quiescence preceding large earthquakes was also observed at the down dip of the 2011 Mw9.1 Tohoku-Oki rupture (Katsumata, 2011). Additionally, the 2021 Kermadec earthquake sequence is likely bounded by along strike barriers caused by forearc structural variation, both to its north and south (K. Lythgoe et al., 2023]. Thus, combining refined earthquake catalog with forearc structure analysis could provide valuable insights into the area of coupled plate interface and hence the potential for future megathrust earthquakes. This could be particularly beneficial for regions lacking dense geodetic observations. Additionally, land areas situated directly above the slab-forearc Moho intersection may experience stronger shaking than traditionally expected. This is because significant coseismic slip could extend deeper into the slab-mantle interface, and intense shaking energy may be radiated from the slab-forearc Moho intersection when the subducting slab is sufficiently cold (e.g., certain regions in South America (Völker et al., 2011)).

Overall, we observe a new type of depth-varying rupture behaviors on the Kermadec subduction interface. Our findings indicate that plate interface beneath the forearc Moho, traditionally considered to be aseismic, have the potential to host earthquakes exceeding magnitude 8. Therefore, we suggest that the seismic hazards in global subduction zones, such as the Mariana where there is ongoing debate regarding the potential of catastrophic large earthquakes (Okal et al., 2013; Uyeda & Kanamori, 1979), should be re-evaluated.

Data Availability Statement

We use the open seismic data from the following seismic networks: AE (Arizona Geological Survey, 2007), AK (Alaska Earthquake Center, 1987), AU (Geoscience Australia, 2021), AT (NOAA, 1967), AV (Alaska Volcano Observatory/USGS, 1988), AZ (Frank Vernon, 1982), BK (Northern California Earthquake Data Center, 2014), C1 (Universidad de Chile, 2012), CC (Cascades Volcano Observatory/USGS, 2001), CI (California Institute of Technology and United States Geological Survey Pasadena, 1926), CN (Natural Resources Canada, 1975), CU (ASL/USGS, 2006), G (IPGP and EOST, 1982), GE (GEOFON Data Centre, 1993), GS (ASL/USGS, 1980), GT (ASL/USGS, 1993), IC (ASL/USGS, 1992), II (Scripps Institution of Oceanography, 1986), IM (Various Institutions, 1965), IU (ASL/USGS, 1988), IW (ASL/USGS, 2003), MX (Red Sísmica Mexicana, n.d.), ND (Centre IRD de Noumea, Nouvelle-Caledonie, 2010), NZ (GNS Science, 2021), OO (Rutgers University, 2013), PY (Frank Vernon, 2014), RM (RIMES Thailand, 2008), S1 (Salmon et al., 2011), SC (New Mexico Tech, 1999), TW (Institute of Earth Sciences, Academia Sinica, Taiwan, 1996), TX (Bureau of Economic Geology, The University of Texas at Bureau of Economic Geology The University of Texas at Austin, 2016), US (ASL/USGS, 1990), UU (University of Utah, 1962), UW (University of Washington, 1963), YW (Hugh Glanville, 2021), C, JP, KG, KS, PS, MY, HK.

References

Abers, G., Van Keken, P., & Hacker, B. (2017). The cold and relatively dry nature of mantle forearcs in subduction zones. *Nature Geoscience*, *10*(5), 333–337. https://doi.org/10.1038/ngeo2922

Alaska Earthquake Center, Univ. of Alaska Fairbanks. (1987). Alaska geophysical network. *International Federation of Digital Seismograph Networks*. [Dataset]. https://doi.org/10.7914/SN/AK

Alaska Volcano Observatory/USGS. (1988). Alaska Volcano Observatory. *International Federation of Digital Seismograph Networks*. [Dataset]. https://doi.org/10.7914/SN/AV

Albuquerque Seismological Laboratory (ASL)/USGS. (1980). US geological Survey networks. *International Federation of Digital Seismograph Networks*. [Dataset]. https://doi.org/10.7914/SN/GS

Albuquerque Seismological Laboratory (ASL)/USGS. (1988). Global seismograph network (GSN - IRIS/USGS). *International Federation of Digital Seismograph Networks*. [Dataset]. https://doi.org/10.7914/SN/IU

Albuquerque Seismological Laboratory (ASL)/USGS. (1990). United States national seismic network. *International Federation of Digital Seismograph Networks*. [Dataset]. https://doi.org/10.7914/SN/US

Albuquerque Seismological Laboratory (ASL)/USGS. (1992). New China digital seismograph network. *International Federation of Digital Seismograph Networks*. [Data set]. https://doi.org/10.7914/SN/IC

Albuquerque Seismological Laboratory (ASL)/USGS. (1993). Global telemetered seismograph network (USAF/USGS). *International Federation of Digital Seismograph Networks*. [Dataset]. https://doi.org/10.7914/SN/GT

Albuquerque Seismological Laboratory (ASL)/USGS. (2003). Intermountain West seismic network. *International Federation of Digital Seismograph Networks*. [Dataset]. https://doi.org/10.7914/SN/IW

Albuquerque Seismological Laboratory (ASL)/USGS. (2006). Caribbean network. *International Federation of Digital Seismograph Networks*. [Dataset]. https://doi.org/10.7914/SN/CU

Arizona Geological Survey. (2007). Arizona broadband seismic network. *International Federation of Digital Seismograph Networks*. [Dataset]. https://doi.org/10.7914/SN/AE

Asano, K., & Iwata, T. (2012). Source model for strong ground motion generation in the frequency range 0.1–10 Hz during the 2011 Tohoku earthquake. *Earth Planets and Space*, *64*(12), 1111–1123. https://doi.org/10.5047/eps.2012.05.003

Avouac, J. P., L. S. Meng, S. J. Wei, T. Wang, and J. P. Ampuero (2015), Lower edge of locked main Himalayan thrust unzipped by the 2015 Gorkha earthquake, *Nature Geoscience*, *8*(9), 708-+, doi:711, https://doi.org/10.1038/Ngeo2518

Bassett, D., Kopp, H., Sutherland, R., Henrys, S., Watts, A. B., Timm, C., et al. (2016). Crustal structure of the Kermadec arc from MANGO seismic refraction profiles. *Journal of Geophysical Research: Solid Earth*, *121*(10), 7514–7546. https://doi.org/10.1002/2016jb013194

Bassett, D., & Watts, A. B. (2015). Gravity anomalies, crustal structure, and seismicity at subduction zones: 1. Seafloor roughness and subducting relief. *Geochemistry, Geophysics, Geosystems*, *16*(5), 1508–1540. https://doi.org/10.1002/2014gc005684

Biemiller, J., Boulton, C., Wallace, L., Ellis, S., Little, T., Mizera, M., et al. (2020). Mechanical implications of creep and partial coupling on the world's fastest slipping low-angle normal fault in southeastern Papua New Guinea. *Journal of Geophysical Research: Solid Earth*, *125*(10), e2020JB020117. https://doi.org/10.1029/2020jb020117

Bureau of Economic Geology, The University of Texas at Austin. (2016). Texas seismological network. *International Federation of Digital Seismograph Networks*. [Dataset]. https://doi.org/10.7914/SN/TX

California Institute of Technology and United States Geological Survey Pasadena. (1926). Southern California seismic network. *International Federation of Digital Seismograph Networks*. [Dataset]. https://doi.org/10.7914/SN/CI

Cascades Volcano Observatory/USGS. (2001). Cascade chain volcano monitoring. *International Federation of Digital Seismograph Networks*. [Dataset]. https://doi.org/10.7914/SN/CC

Centre IRD de Noumea, & Nouvelle-Caledonie (2010). New Caledonia broadband seismic network. *International Federation of Digital Seismograph Networks*. [Dataset]. https://doi.org/10.7914/SN/ND

Christensen, D. H., & Ruff, L. J. (1988). Seismic coupling and outer rise earthquakes. *Journal of Geophysical Research*, *93*(B11), 13421–13444. https://doi.org/10.1029/jb093ib11p13421

Contreras-Reyes, E., Grevemeyer, I., Watts, A. B., Flueh, E. R., Peirce, C., Moeller, S., & Papenberg, C. (2011). Deep seismic structure of the Tonga subduction zone: Implications for mantle hydration, tectonic erosion, and arc magmatism. *Journal of Geophysical Research*, *116*(B10), B10103. https://doi.org/10.1029/2011jb008434

DeMets, C., Gordon, R. G., & Argus, D. F. (2010). Geologically current plate motions. *Geophysical Journal International*, *181*(1), 1–80. https://doi.org/10.1111/j.1365-246x.2009.04491.x

Dziewonski, A. M., Chou, T. A., & Woodhouse, J. H. (1981). Determination of earthquake source parameters from waveform data for studies of global and regional seismicity. *Journal of Geophysical Research*, *86*(B4), 2825–2852. https://doi.org/10.1029/jb086ib04p02825

Ekstrom, G., Nettles, M., & Dziewonski, A. M. (2012). The global CMT project 2004-2010: Centroid-moment tensors for 13,017 earthquakes. *Physics of the Earth and Planetary Interiors*, *200*, 1–9. https://doi.org/10.1016/j.pepi.2012.04.002

Escartin, J., Hirth, G., & Evans, B. (2001). Strength of slightly serpentinized peridotites: Implications for the tectonics of oceanic lithosphere. *Geology*, *29*(11), 1023–1026. https://doi.org/10.1130/0091-7613(2001)029<1023:sosspi>2.0.co;2

Evans, B. W. (2004). The serpentinite multisystem revisited: Chrysotile is metastable. *International Geology Review*, *46*(6), 479–506. https://doi.org/10.2747/0020-6814.46.6.479

Frank, V. (2014). Piñon flats observatory array. *International Federation of Digital Seismograph Networks*. [Dataset]. https://doi.org/10.7914/SN/PY

Frank Vernon. (1982). ANZA regional network. *International Federation of Digital Seismograph Networks*. [Dataset]. https://doi.org/10.7914/SN/AZ

Gao, X., & Wang, K. (2014). Strength of stick-slip and creeping subduction megathrusts from heat flow observations. *Science*, *345*(6200), 1038–1041. https://doi.org/10.1126/science.1255487

GEOFON Data Centre. (1993). GEOFON seismic network. *GFZ Data Services*. [Dataset]. https://doi.org/10.14470/TR560404

Geoscience Australia. (2021). Australian national seismograph network data collection (version 2.0, September 2018). *Commonwealth of Australia (Geoscience Australia)*. https://doi.org/10.26186/144675

GNS Science. (2021). GeoNet Aotearoa New Zealand seismic digital waveform dataset. *GNS Science*. [Dataset]. https://doi.org/10.21420/G19Y-9D40

Hacker, B. R., Abers, G. A., & Peacock, S. M. (2003). Subduction factory 1. Theoretical mineralogy, densities, seismic wave speeds, and H2O contents. *Journal of Geophysical Research*, *108*(B1). https://doi.org/10.1029/2001jb001127

Hayes, G. P., Moore, G. L., Portner, D. E., Hearne, M., Flamme, H., Furtney, M., & Smoczyk, G. M. (2018). Slab2, a comprehensive subduction zone geometry model. *Science*, *362*(6410), 58–61. https://doi.org/10.1126/science.aat4723

Huang, Y. H., Meng, L. S., & Ampuero, J. P. (2012). A dynamic model of the frequency-dependent rupture process of the 2011 Tohoku-Oki earthquake. *Earth Planets and Space*, *64*(12), 1061–1066. https://doi.org/10.5047/eps.2012.05.011

Hugh Glanville. (2021). Muswellbrook. *International Federation of Digital Seismograph Networks*. [Dataset]. https://doi.org/10.7914/SN/YW_2021

Hyndman, R. D., & Peacock, S. M. (2003). Serpentinization of the forearc mantle. *Earth and Planetary Science Letters*, *212*(3–4), 417–432. https://doi.org/10.1016/s0012-821x(03)00263-2

Hyndman, R. D., Yamano, M., & Oleskevich, D. A. (1997). The seismogenic zone of subduction thrust faults. *Island Arc*, *6*(3), 244–260. https://doi.org/10.1111/j.1440-1738.1997.tb00175.x

Institut de physique du globe de Paris (IPGP), and École et Observatoire des Sciences de la Terre de Strasbourg (EOST). (1982). *GEOSCOPE, French Global Network of broad band seismic stations*. Institut de physique du globe de Paris (IPGP), Université de Paris. https://doi.org/10.18715/GEOSCOPE

Institute of Earth Sciences, Academia Sinica, Taiwan. (1996). Broadband array in Taiwan for seismology. *International Federation of Digital Seismograph Networks*. [Dataset]. https://doi.org/10.7914/SN/TW

Ishii, M., Shearer, P. M., Houston, H., & Vidale, J. E. (2005). Extent, duration and speed of the 2004 Sumatra-Andaman earthquake imaged by the Hi-Net array. *Nature*, *435*(7044), 933–936. https://doi.org/10.1038/nature03675

Ji, C., Wald, D. J., & Helmberger, D. V. (2002). Source description of the 1999 Hector Mine, California, earthquake, part I: Wavelet domain inversion theory and resolution analysis. *Bulletin of the Seismological Society of America*, *92*(4), 1192–1207.

Kaproth, B. M., & Marone, C. (2013). Slow earthquakes, preseismic velocity changes, and the origin of slow frictional stick-slip. *Science*, *341*(6151), 1229–1232. https://doi.org/10.1126/science.1239577

Katsumata, K. (2011). A long-term seismic quiescence started 23 years before the 2011 off the Pacific coast of Tohoku Earthquake (M= 9.0). *Earth Planets and Space*, *63*(7), 709–712. https://doi.org/10.5047/eps.2011.06.033

Kodaira, S., Iidaka, T., Kato, A., Park, J.-O., Iwasaki, T., & Kaneda, Y. (2004). High pore fluid pressure may cause silent slip in the Nankai Trough. *Science*, *304*(5675), 1295–1298. https://doi.org/10.1126/science.1096535

Lay, T., Astiz, L., Kanamori, H., & Christensen, D. H. (1989). Temporal variation of large intraplate earthquakes in coupled subduction zones. *Physics of the Earth and Planetary Interiors*, *54*(3–4), 258–312. https://doi.org/10.1016/0031-9201(89)90247-1

Lay, T., Kanamori, H., Ammon, C. J., Hutko, A. R., Furlong, K., & Rivera, L. (2009). The 2006–2007 Kuril Islands great earthquake sequence. *Journal of Geophysical Research*, *114*(B11). https://doi.org/10.1029/2008jb006280

Lay, T., Kanamori, H., Ammon, C. J., Koper, K. D., Hutko, A. R., Ye, L., et al. (2012). Depth-varying rupture properties of subduction zone megathrust faults. *Journal of Geophysical Research*, *117*(B4). https://doi.org/10.1029/2011jb009133

Lythgoe, K., Bradley, K., Zeng, H., & Wei, S. (2023). Persistent asperities at the Kermadec subduction zone controlled by changes in forearc structure: 1976 and 2021 doublet earthquakes. *Earth and Planetary Science Letters*, *624*, 118465. https://doi.org/10.1016/j.epsl.2023.118465

Lythgoe, K., Muzli, M., Bradley, K., Wang, T., Nugraha, A. D., Zulfakriza, Z., et al. (2021). Thermal squeezing of the seismogenic zone controlled rupture of the volcano-rooted Flores Thrust. *Science Advances*, *7*(5), eabe2348. https://doi.org/10.1126/sciadv.abe2348

Ma, B., Geersen, J., Lange, D., Klaeschen, D., Grevemeyer, I., Contreras-Reyes, E., et al. (2022). Megathrust reflectivity reveals the updip limit of the 2014 Iquique earthquake rupture. *Nature Communications*, *13*(1), 3969. https://doi.org/10.1038/s41467-022-31448-4

Meng, L. S., Inbal, A., & Ampuero, J.-P. (2011). A window into the complexity of the dynamic rupture of the 2011 Mw 9 Tohoku-Oki earthquake. *Geophysical Research Letters*, *38*(7). https://doi.org/10.1029/2011gl048118

Miura, S., Takahashi, N., Nakanishi, A., Tsuru, T., Kodaira, S., & Kaneda, Y. (2005). Structural characteristics off Miyagi forearc region, the Japan Trench seismogenic zone, deduced from a wide-angle reflection and refraction study. *Tectonophysics*, *407*(3–4), 165–188. https://doi.org/10.1016/j.tecto.2005.08.001

Moore, D. E., & Lockner, D. A. (2013). Chemical controls on fault behavior: Weakening of serpentinite sheared against quartz-bearing rocks and its significance for fault creep in the San Andreas system. *Journal of Geophysical Research: Solid Earth*, *118*(5), 2558–2570. https://doi.org/10.1002/jgrb.50140

Moore, J. C., & Vrolijk, P. (1992). Fluids in accretionary prisms. *Reviews of Geophysics*, *30*(2), 113–135. https://doi.org/10.1029/92rg00201

Moreno, M., Li, S., Melnick, D., Bedford, J., Báez, J. C., Motagh, M., et al. (2018). Chilean megathrust earthquake recurrence linked to frictional contrast at depth. *Nature Geoscience*, *11*(4), 285–290. https://doi.org/10.1038/s41561-018-0089-5

Müller, R. D., Sdrolias, M., Gaina, C., & Roest, W. R. (2008). Age, spreading rates, and spreading asymmetry of the world's ocean crust. *Geochemistry, Geophysics, Geosystems*, *9*(4). https://doi.org/10.1029/2007gc001743

Natural Resources Canada. (1975). Canadian national seismograph network. *Natural Resources Canada*. [Dataset]. https://doi.org/10.7914/SN/CN

New Mexico Tech. (1999). New Mexico Tech seismic network. *International Federation of Digital Seismograph Networks*. [Dataset]. https://doi.org/10.7914/0abk-1345

NOAA National Oceanic and Atmospheric Administration (USA). (1967). National tsunami warning center Alaska seismic network. *International Federation of Digital Seismograph Networks*. [Dataset]. https://doi.org/10.7914/SN/AT

Northern California Earthquake Data Center. (2014). Berkeley digital seismic network (BDSN). Northern California Earthquake Data Center. [Dataset]. https://doi.org/10.7932/BDSN

Okal, E. A., Reymond, D., & Hongsresawat, S. (2013). Large, pre-digital earthquakes of the Bonin-Mariana subduction zone, 1930–1974. *Tectonophysics*, *586*, 1–14. https://doi.org/10.1016/j.tecto.2012.09.006

Oleskevich, D., Hyndman, R., & Wang, K. (1999). The updip and downdip limits to great subduction earthquakes: Thermal and structural models of Cascadia, south Alaska, SW Japan, and Chile. *Journal of Geophysical Research*, *104*(B7), 14965–14991. https://doi.org/10.1029/1999jb900060

Omuralieva, A. M., Hasegawa, A., Matsuzawa, T., Nakajima, J., & Okada, T. (2012). Lateral variation of the cutoff depth of shallow earthquakes beneath the Japan Islands and its implications for seismogenesis. *Tectonophysics*, *518*, 93–105. https://doi.org/10.1016/j.tecto.2011.11.013

Power, W., Wallace, L., Wang, X., & Reyners, M. (2012). Tsunami hazard posed to New Zealand by the Kermadec and southern New Hebrides subduction margins: An assessment based on plate boundary kinematics, interseismic coupling, and historical seismicity. *Pure and Applied Geophysics*, *169*(1), 1–36. https://doi.org/10.1007/s00024-011-0299-x

Red Sísmica Mexicana. (n.d.). https://doi.org/10.21766/SSNMX/SN/MX

Regional Integrated Multi-Hazard Early Warning System (RIMES Thailand). (2008). Regional integrated multi-hazard early warning system. *International Federation of Digital Seismograph Networks*. [Dataset]. https://doi.org/10.7914/SN/RM

Romano, F., Gusman, A. R., Power, W., Piatanesi, A., Volpe, M., Scala, A., & Lorito, S. (2021). Tsunami source of the 2021 MW 8.1 Raoul Island earthquake from DART and tide-gauge data inversion. *Geophysical Research Letters*, *48*(17), e2021GL094449. https://doi.org/10.1029/2021gl094449

Ruiz, S., Metois, M., Fuenzalida, A., Ruiz, J., Leyton, F., Grandin, R., et al. (2014). Intense foreshocks and a slow slip event preceded the 2014 Iquique M w 8.1 earthquake. *Science*, *345*(6201), 1165–1169. https://doi.org/10.1126/science.1256074

Rutgers University. (2013). Ocean observatories initiative. *International Federation of Digital Seismograph Networks*. [Dataset]. https://doi.org/10.7914/SN/OO

Sallarès, V., & Ranero, C. R. (2019). Upper-plate rigidity determines depth-varying rupture behaviour of megathrust earthquakes. *Nature*, *576*(7785), 96–101. https://doi.org/10.1038/s41586-019-1784-0

Salmon, M., Balfour, N., & Sambridge, M. (2011). Australian seismometers in schools. *AusPass*. [Dataset]. https://doi.org/10.7914/SN/S1

Schwartz, S., Guillot, S., Reynard, B., Lafay, R., Debret, B., Nicollet, C., et al. (2013). Pressure–temperature estimates of the lizardite/antigorite transition in high pressure serpentinites. *Lithos*, *178*, 197–210. https://doi.org/10.1016/j.lithos.2012.11.023

Scripps Institution of Oceanography. (1986). Global seismograph network - IRIS/IDA. *International Federation of Digital Seismograph Networks*. [Dataset]. https://doi.org/10.7914/SN/II

Shillington, D. J., Bécel, A., & Nedimović, M. R. (2022). Upper plate structure and megathrust properties in the Shumagin Gap near the July 2020 M7. 8 Simeonof event. *Geophysical Research Letters*, *49*(2), e2021GL096974. https://doi.org/10.1029/2021gl096974

Sibson, R. H. (1983). Continental fault structure and the shallow earthquake source. *Journal of the Geological Society*, *140*(5), 741–767. https://doi.org/10.1144/gsjgs.140.5.0741

Simons, M., Minson, S. E., Sladen, A., Ortega, F., Jiang, J., Owen, S. E., et al. (2011). The 2011 magnitude 9.0 Tohoku-Oki earthquake: Mosaicking the megathrust from seconds to centuries. *Science*, *332*(6036), 1421–1425. https://doi.org/10.1126/science.1206731

Stratford, W., Peirce, C., Paulatto, M., Funnell, M., Watts, A., Grevemeyer, I., & Bassett, D. (2015). Seismic velocity structure and deformation due to the collision of the Louisville Ridge with the Tonga-Kermadec Trench. *Geophysical Journal International*, *200*(3), 1503–1522. https://doi.org/10.1093/gji/ggu475

Uchida, N., & Bürgmann, R. (2021). A decade of lessons learned from the 2011 Tohoku-Oki earthquake. *Reviews of Geophysics*, *59*(2), e2020RG000713. https://doi.org/10.1029/2020rg000713

Universidad de Chile. (2012). Red Sismologica nacional. *International Federation of Digital Seismograph Networks*. [Dataset]. https://doi.org/10.7914/SN/C1

University of Utah. (1962). University of Utah regional seismic network. *International Federation of Digital Seismograph Networks*. [Dataset]. https://doi.org/10.7914/SN/UU

University of Washington. (1963). Pacific Northwest seismic network - university of Washington. *International Federation of Digital Seismograph Networks*. [Dataset]. https://doi.org/10.7914/SN/UW

Uyeda, S., & Kanamori, H. (1979). Back-arc opening and the mode of subduction. *Journal of Geophysical Research*, *84*(B3), 1049–1061. https://doi.org/10.1029/jb084ib03p01049

Various Institutions. (1965). International miscellaneous stations. *International Federation of Digital Seismograph Networks*. [Dataset]. https://doi.org/10.7914/vefq-vh75

Völker, D., Grevemeyer, I., Stipp, M., Wang, K., & He, J. (2011). Thermal control of the seismogenic zone of southern central Chile. *Journal of Geophysical Research*, *116*(B10), B10305. https://doi.org/10.1029/2011jb008247

Wang, K., Huang, T., Tilmann, F., Peacock, S. M., & Lange, D. (2020). Role of Serpentinized mantle wedge in affecting Megathrust Seismogenic behavior in the area of the 2010 M= 8.8 Maule earthquake. *Geophysical Research Letters*, *47*(22), e2020GL090482. https://doi.org/10.1029/2020gl090482

Wang, K., Luo, H., He, J., & Carvajal, M. (2025). Soft barrier to megathrust rupture enabled by serpentinized mantle wedge: The Chile subduction zone. *Earth and Planetary Science Letters*, *650*, 119115. https://doi.org/10.1016/j.epsl.2024.119115

Wang, X., Bradley, K. E., Wei, S., & Wu, W. (2018). Active backstop faults in the Mentawai region of Sumatra, Indonesia, revealed by teleseismic broadband waveform modeling. *Earth and Planetary Science Letters*, *483*, 29–38. https://doi.org/10.1016/j.epsl.2017.11.049

Wang, X., Wei, S., & Letters, W.-W. (2017). Double-ramp on the Main Himalayan Thrust revealed by broadband waveform modeling of the 2015 Gorkha earthquake sequence. *Earth and Planetary Science Letters*, *473*, 83–93. https://doi.org/10.1016/j.epsl.2017.05.032

Wang, X., Wei, S., Morales-Yáñez, C., Duputel, Z., Chen, L., Hao, T., & Zhao, L. (2024). Plate interface geometry complexity and persistent heterogenous coupling revealed by a high-resolution earthquake focal mechanism catalog in Mentawai, Sumatra. *Earth and Planetary Science Letters*, *637*, 118726. https://doi.org/10.1016/j.epsl.2024.118726

Yao, H., Shearer, P. M., & Gerstoft, P. (2013). Compressive sensing of frequency-dependent seismic radiation from subduction zone megathrust ruptures. *Proceedings of the National Academy of Sciences*, *110*(12), 4512–4517. https://doi.org/10.1073/pnas.1212790110

Yin, J., Yang, H., Yao, H., & Weng, H. (2016). Coseismic radiation and stress drop during the 2015 Mw 8.3 Illapel, Chile megathrust earthquake. *Geophysical Research Letters*, *43*(4), 1520–1528. https://doi.org/10.1002/2015gl067381

Yuan, X., Sobolev, S. V., Kind, R., Oncken, O., Bock, G., Asch, G., et al. (2000). Subduction and collision processes in the Central Andes constrained by converted seismic phases. *Nature*, *408*(6815), 958–961. https://doi.org/10.1038/35050073

Zeng, H., Wei, S., & Rosakis, A. (2022). A travel-time path calibration strategy for back-projection of large earthquakes and its application and validation through the segmented super-shear rupture imaging of the 2002 Mw 7.9 Denali earthquake. *Journal of Geophysical Research: Solid Earth*, *127*(6), e2022JB024359. https://doi.org/10.1029/2022jb024359